Constraining clouds and convective parameterizations in a climate model using paleoclimate data

R. D. Ramos[1], A. N. LeGrande[2], M. L. Griffiths[1], G. S., Elsaesser[2,3], D. T. Litchmore[2,3], J. E. Tierney[4], F. S. R. Pausata[5] and J. Nusbaumer[6]

[1]Department of Environmental Science, William Paterson University, Wayne, NJ, USA.

[2]NASA Goddard Institute for Space Studies, New York, NY, USA.

[3]Columbia University, New York, NY, USA.

[4]Department of Geosciences, The University of Arizona, Tucson, AZ, USA.

[5]Department of Earth and Atmosphere Sciences, University of Quebec in Montreal, Montreal, Canada

[6]Climate and Global Dynamics Laboratory, National Center for Atmospheric Research, Boulder, CO, USA.

Corresponding author: Riovie Ramos (ramosr34@wpunj.edu); Allegra N. LeGrande (allegra.n.legrande@nasa.gov); Michael L. Griffiths (griffithsm@wpunj.edu)

Key Points:

- Paleoclimate relative to modern are more parameter sensitive, allowing for an assessment of uncertainties over a variety of climate forcing
- Certain simulations reproduced the $\delta^{18}O$ of precipitation from paleoclimate proxies better than the default parameterization
- No single set of parameters works well in all climate states likely due to varying boundary conditions influencing cloud feedbacks

Abstract

Cloud and convective parameterizations strongly influence uncertainties in equilibrium climate sensitivity (ECS). We provide a proof-of-concept study to constrain these parameterizations in a perturbed parameter ensemble of the atmosphere-only version of the Goddard Institute for Space Studies (GISS) Model E2.1 simulations by evaluating model biases in the present-day runs using multiple satellite climatologies and by comparing simulated $\delta^{18}O$ of precipitation ($\delta^{18}O_p$), known to be sensitive to parameterization schemes, with a global database of speleothem $\delta^{18}O$ records covering the Last Glacial Maximum (LGM), mid-Holocene (MH) and pre-industrial (PI) periods. Relative to modern interannual variability, paleoclimate simulations show greater sensitivity to parameter changes, allowing for an evaluation of model uncertainties over a broader range of climate forcing and the identification of parts of the world that are parameter sensitive. Certain simulations reproduced absolute $\delta^{18}O_p$ values across all time periods, along with LGM and MH $\delta^{18}O_p$ anomalies relative to the PI, better than the default parameterization. No single set of parameterizations worked well in all climate states, likely due to the non-stationarity of cloud feedbacks under varying boundary conditions. Future work that involves varying multiple parameter sets simultaneously with coupled ocean feedbacks will likely provide improved constraints on cloud and convective parameterizations.

Plain Language Summary

Equilibrium climate sensitivity (ECS) is a key climate metric that quantifies the rise in global mean surface temperature in response to doubling of atmospheric CO_2. Changes in hydroclimate, temperature extremes, and other aspects of future climate projections are closely tied to a model's ECS. For decades, ECS range has remained wide despite improvements from using

multiple lines of evidence. One persistent source of this spread is related to cloud and convective processes, which occur at scales too small to be explicitly resolved, and thus require parameterizations to be represented in climate models. These parameterizations directly influence water isotopes by modulating simulated clouds and atmospheric circulation, and thus can be used to constrain model processes and identify model biases. In this work, we demonstrated that paleoclimate simulations are more parameter sensitive than the modern, highlighting the potential of past climates in discriminating cloud and convective parameterizations. Using satellite- and proxy-model comparisons, we identified the top performing parameterizations which differ for each time period likely due to varying cloud feedbacks under diverse climatic forcing. Overall, our results provide a framework for fine-tuning model representations using combined paleoclimate and satellite data, offering a unique opportunity to assess model uncertainties over a broader range of climate variability.

1 Introduction

Cloud and convective processes vary at scales significantly smaller than a general circulation model (GCM) grid box, requiring them to be parameterized on simulated grid-scale variables (Boucher *et al.*, 2013). Because such parameterizations employ different assumptions (Lopez, 2007), representation of cloud and convective effects in climate models inherently hold large uncertainties. Cloud and convective parameterizations, aside from aerosol schemes and aerosol-cloud interactions (Meehl *et al.*, 2020), are considered the leading source of inter-model spread in equilibrium climate sensitivity (ECS) estimates (Dufresne and Bony, 2008; Sherwood *et al.*, 2014; Webb *et al.*, 2015; Zelinka *et al.*, 2020) and consequently the broad range of future climate projections (Flato *et al.*, 2013; Sherwood *et al.*, 2014). The latest generation of climate models participating in Coupled Model Intercomparison Project Phase 6 (CMIP6) have an average ECS value of 3.9°C and range from 1.8°C to 5.6°C (Zelinka *et al.*, 2020), which is higher and more variable than the CMIP5 models (i.e., mean of 3.3°C and range of 1.5°C to 4.5°C (Flato *et al.*, 2013; Knutti *et al.*, 2017)) and estimates from the Intergovernmental Panel on Climate Change Assessment Report 6 (i.e., mean of 3°C with a very likely range of 2°C to 5 °C, (IPCC, 2021; Hausfather *et al.*, 2022).

Paleoclimate evidence provides additional constraints on ECS by offering an independent test of climate model performance. Colder and warmer intervals of well-known forcings and fairly stable climate states relative to the present instrumental period such as the Last Glacial Maximum (LGM; 21 ka or kilo-years before present) and the mid-Pliocene warm period (mPWP; 3.3-3.0 Ma or million years before present) indicate an ECS range of 1.5°C to 5°C with a maximum likelihood of 2.5°C (Sherwood *et al.*, 2020). Based on temperature changes provided by paleorecords and known responses to climate forcings during these time periods, these joint yet independent paleoconstraints on ECS argue against extreme estimates of 1.2°C and greater than 6°C (Sherwood *et al.*, 2014; Zhu and Poulsen, 2020). In another example, proxy-model comparison using the Community Earth System Model version 2 (CESM2) – one such model that reports an ECS greater than 5°C in the CMIP6 models – reveals that their simulated LGM cooling is excessive and not realistic relative to proxy reconstructions and previous model simulations, highlighting the cloud feedback-related source of their overestimated ECS (Zhu *et al.*, 2021). While these studies demonstrate the strong potential of past climates in constraining ECS, evaluating the uncertainties directly related to cloud and convective parameterizations remains limited to a qualitative ruling out of high ECS.

A perturbed parameter ensembles (PPE) experiment, which creates different versions of a climate model by systematically changing a parameter value within a reasonable range, is particularly useful in assessing the degree to which uncertainties are explained by parameter choices. Typically, clouds and convective parameterizations are chosen based on the bias score between climate model output and observational datasets, usually derived from satellite remote sensing platforms that began observing ~3 decades ago (Mauritsen *et al.*, 2012; Galewsky *et al.*, 2016). However, in the context of future climate change, these observational datasets only offer a fraction of the range of climate change projected over the next 100 years. Finding ways to constrain these choices on a broader variety of climates is thus desirable. Moreover, in a traditional PPE approach, models are not typically re-tuned into radiative balance after altering a single tuning parameter (Schmidt *et al.*, 2017), which may have important implications in resolving or revealing biases from previous compensating errors (Collins *et al.*, 2011). However, not much is known whether this tuning approach after each parameter change is preferable especially when considering a broader range of climate states.

Widely observed through satellites and preserved on various paleoclimate archives, water isotopes provide a common means to understand present and past climates. Water isotopes serve as integrative tracers of the hydrologic cycle due to molecular differences in mass that drive fractionation during water phase changes. In the atmosphere, the variability in the oxygen isotopic composition of precipitation ($\delta^{18}O_P$) is driven by several local and non-local processes including the origin and initial isotopic composition of the water vapor in an air parcel, amount of rainout, evaporation of rainfall, seasonality and temperature history, and mixing with other air parcels (Dansgaard, 1964; Gat, 1996; Noone, 2008; Galewsky *et al.*, 2016). Increasingly incorporating water isotopes in model simulations has significantly advanced our understanding of the mechanisms that govern their variability across broader spatiotemporal scales (Galewsky *et al.*, 2016).

Previous studies have demonstrated the sensitivity of water isotope ratios to perturbations in cloud and convective parameterizations in isotope enabled GCMs, signifying their utility in evaluating model performance and potentially identifying model biases (Schmidt *et al.*, 2005; Bony *et al.*, 2008; Lee *et al.*, 2009; Bolot *et al.*, 2013; Field *et al.*, 2014; Nusbaumer *et al.*, 2017). For example, excessive diffusive advection and high convection frequency were shown to cause significant model biases in the isotope enabled Laboratoire de Météorologie Dynamique Zoomed version 4 (LMDZ4, (Risi *et al.*, 2012) and Community Atmosphere Model version 5 (CAM5, (Nusbaumer *et al.*, 2017) models, respectively. In the atmosphere-only version of Goddard Institute for Space Studies (GISS) Model E2, water isotopes were found to be more sensitive to parameter changes than traditional diagnostics such as precipitation and temperature, likely related to cumulus entrainment strength (Field *et al.*, 2014). These models were compared against modern water isotope observations from satellites (e.g., Aura Tropospheric Emission Spectrometer (TES), (Worden *et al.*, 2007); Scanning Imaging Absorption Spectrometer for Atmospheric Cartography (SCIAMACHY), (Frankenberg *et al.*, 2009)), providing a spatially robust means of constraining model results.

Variability in water isotopes may also be obtained from various paleoclimate archives that are not only spatially well-distributed but are also available across past earth climates drastically different from today. One excellent source of past water isotope variability and therefore hydroclimatic information are speleothems. Speleothems are secondary cave deposits that form from dissolution of carbonate bedrock through water action. While their geographical distribution is largely constrained by the geology of a region, speleothems form under a broad range of hydroclimatic regimes ideal for investigating predominant regional patterns. Variations in speleothem δ^{18}O largely reflects the δ^{18}O of soil ($\delta^{18}O_s$) and groundwater percolation, which in turn is heavily influenced by $\delta^{18}O_p$ above the cave and other processes within the karst system (Lachniet, 2009; Fairchild and Baker, 2012). Early speleothem δ^{18}O compilations and the more recently available Speleothem Isotope Synthesis and Analysis (SISAL) database (Atsawawaranunt *et al.*, 2018; Comas-Bru *et al.*, 2020, 2019), a large global compilation of speleothem isotope records since the last glacial, have aided in evaluating GCM performance across the LGM and mid-Holocene (MH; 6ka) time periods (Caley *et al.*, 2014; Werner *et al.*, 2016; Cauquoin *et al.*, 2019; Comas-Bru *et al.*, 2019) and have served as an independent validation check in reconstructions of glacial temperature fields (Tierney *et al.*, 2020a), demonstrating their usefulness in benchmarking isotope enabled paleoclimate simulations. However, not all parts of the world are equally influenced by cloud and convective parameter changes, implying that proxy record locations may be more or less constraining against simulations. This has not been fully quantified in existing paleoproxy-model comparisons and/or analyses of model-satellite discrepancies both globally and restricted to proxy sites only.

In this study, we explore cloud and convective parameterizations (Table 1) in the GISS-E2.1 climate model (Kelley *et al.*, 2020) that likely have a significant impact on water isotope distribution and ECS. We use two sets of atmosphere-only simulations: one that has been re-tuned into radiative equilibrium in the pre-industrial (hereafter referred to as the balanced version as per (Schmidt *et al.*, 2017)) and another which only changes the parameters (hereafter referred to as the unbalanced version), to evaluate whether this approach is preferable in simulations of past climates with large differences in radiative forcing. We investigate the variability and sensitivity of key climate variables to cloud and convective changes and identify parameter-sensitive sites in the present-day (PD, year 2000) and paleoclimate simulations covering the pre-industrial (PI, year 1850), MH and LGM periods. We also compare and evaluate the model simulations against multiple satellite climatologies and assess the agreement between simulated $\delta^{18}O_p$ and speleothem $\delta^{18}O$ from the SISAL version 2 (Comas-Bru *et al.*, 2020) database. This proof-of-concept study presents a basis to which we determine the best suite of parameters representing clouds and convective processes across distinct time periods, critical in improving isotope-enabled models and thus, ECS and climate projections.

Table 1. Parameter space exploration of GISS-E2.1.

Short Name	Parameter	Description	GISS-E2.1 default	New Value	Mean Surface Air Temperature, °C (global, NH, SH)	M Precip mm (global,
std	standard	----	----	----	13.90,14.34,13.65	2.96,2
rev	rain re-evaporation above cloud base	Allows extra moistening above the cloud base, increasing moisture availability and model precipitation as well as global temperature	On (1)	Off (0)	13.78,14.03,13.52	2.94,2
entr50-50 *entr60-40* *entr20-80*	entrainment rate for plume (1 & 2)	Modulates relative size and dilution of (2 max per grid cell per level) convective plumes by setting how much mass is entrained into each of the less- (deep) and more-entraining (shallow) convective plumes, setting up moisture availability for each for precipitation and convection depth	0.4; 0.6	0.5; 0.5 0.6; 0.4 0.2; 0.8	13.98.14.30,13.66 14.00,14.33,13.67 14.00,14.36,13.65	2.98,2 2.95,2 2.92,2
tconvadjX2	convection adjustment time	Modulates time for convective mass to reach the tropopause; thus the response time of temperature and moisture profiles to adjust to moist convective processes	1	2	14.03,14.35,13.72	2.96,2
trigger1.1 *trigger1.2* *trigger0.99* *trigger1.3* *trigger1.0*	convective trigger	Changes convection initiation (easier or harder to attain) by the relative balance of stable layers against planetary boundary layer processes (turbulent lifting, near-surface stability variation, moisture), vertical wind shear, mesoscale ascent, and gravity waves	2	1.1 1.2 0.99 1.3 1.0	14.02,14.36,13.67 13.99,14.35,13.65 13.95,14.27,13.63 13.99,14.35,13.63 13.94,14.25,13.63	2.98,2 2.98,2 3.09,2 2.98,2 2.98,2
droprad50-50 *droprad50-130* *droprad130-50* *droprad30-130*	cloud droplet radius (liquid- ice)	Liquid droplet and ice particle sizes for a given condensate amount. Smaller sizes are relatively reflective (shortwave scattering, thus increasing reflected SW radiation) versus insulating (longwave absorption and re-emission)	1; 1	0.5; 0.5 0.5; 1.3 1.3; 0.5 1.3; 1.3	13.88,14.13,13.62 14.16,14.55,13.77 13.74,14.97,13.50 14.02,14.40,13.65	2.98,2 2.98,2 2.93,2 2.98,2
critQ2-2 *critQ1-0.5* *critQ1-4* *critQ2-4*	critical cloud water content (liquid & ice)	The (critical) threshold controlling amount of water converted to precipitation via auto-conversion. Higher means more cloud condensate and more optically thick clouds often altering radiation, but lowering precipitation	2; 1	2; 2 1; 0.5 1; 4 2; 4	13.99,14.33,13.65 14.00,14.30,13.69 13.95,14.30,13.61 13.96,14.28,13.65	2.95,2 2.99,2 2.96,2 2.95,2

2 Materials and Methods

2.1 NASA GISS E2.1

Simulations were conducted using the atmosphere-only GISS-E2.1, a CMIP6 submission described in length in Kelley et al. (2020). Relative to GISS-E2 (Schmidt *et al.*, 2014), the default E2.1 configuration has an improved treatment of mixed-phase clouds, improvements in the planetary boundary layer parameterization, and systematic increases in convective entrainment rates (Kelley *et al.*, 2020), though these rates are perturbed as part of this study as detailed below.

Water tracers ($^{1}H_2{}^{16}O$, "normal" water; $^{2}H^{1}H^{16}O$, δD; and $^{1}H_2{}^{18}O$, $\delta^{18}O$; where permil (‰) $\delta \equiv 1000 * [(R_{std}/R_{smow})-1]$) were included in the land surface, sea ice, sea surface, and atmosphere. These isotopes are tracked through all stages of the water cycle and are advected like water through the model with appropriate fractionation during each phase change (Schmidt *et al.*, 2005, 2007; LeGrande and Schmidt, 2009) .

2.2 Time slice experiments

We performed three paleo-time slice experiments as described for the LGM (Kageyama *et al.*, 2021, 2017), MH (Otto-Bliesner *et al.*, 2017; Brierley *et al.*, 2020) and PI (Eyring *et al.*, 2016). These followed the Paleoclimate Modelling and Intercomparison Project (PMIP4) and CMIP6 protocols (Kageyama *et al.*, 2017; Otto-Bliesner *et al.*, 2017). For each time slice, appropriate changes to topography, bathymetry, and land-ocean-ice mask (LGM: Glac1D, Tarasov and Peltier, 2002; Tarasov *et al.*, 2012; Abe-Ouchi *et al.*, 2013; Briggs *et al.*, 2014); river routing (Licciardi *et al.*, 1998, 1999; Peltier, 2004); vegetation cover (Ray and Adams, 2001); orbital changes (Berger and Loutre, 1991); greenhouse gases (Indermühle *et al.*, 1999);

standard mean ocean water, salinity and water isotopes (Adkins and Schrag, 2003) were made (Table 2). All these runs were completed to surface equilibrium in GISS-E2.1-G (Kelley *et al.*, 2020); the surface sea ice fraction, sea ice thickness, and sea surface temperatures were then recorded. Coupled simulations are computationally expensive, and thus, surface conditions were used in this proof-of-concept study to drive a new suite of GISS-E2.1 simulation (CMIP6) in atmosphere-only mode with the same forcing conditions to create the LGM, MH and PI runs. We conduct one further present-day (PD) experiment to facilitate comparison with the satellite products, using year 2000 atmospheric constituents and a climatological mean from Hadley for 2000-2015 for ocean surface conditions (Table 2). Each experiment was run for 21 years, with the first year left out so the atmosphere equilibrates with the surface conditions; we used the last two decadal outputs as the basis of all presented results and interpretations.

Table 2. Summary of forcing and boundary conditions for each time slice experiment. All experiments applied topography, bathymetry, land-ocean-ice mask, greenhouse gas, river routing and appropriate SMOW changes.

Time slice	**Ice sheet**	**SST/SICE**	**GHG**	**Mean salinity, psu**	**SMOW (δ^{18}O, δD)**
Present Day (PD)	modern	Hadley Obs	year 2000	34.7	0‰, 0‰
PI, 1850	modern	CMIP6: PI	year 1850	34.7	0‰, 0‰
MH, 6 ka	modern	CMIP6: MH	6 ka	34.7	0‰, 0‰
LGM, 21 ka	Glac1D	CMIP6: LGM	21 ka	35.7	1.0‰, 8.0‰

2.3 Cloud and convective parameterizations and model tuning

GISS-E2.1 regularly uses five tuning parameters (Kelley *et al.*, 2020). Here, we re-balanced the model by altering cloud reflectivity (Schmidt *et al.*, 2017), after each parameter change to ensure that the decadal top of the atmosphere net planetary radiation is within 0.2 W/m^2 during a pre-industrial simulation (i.e., balanced version). We conduct a parallel set of experiments where this tuning was not done (i.e., unbalanced version) to check that the tuning itself is not influencing our interpretation. Ideally, this positions us to complete fully coupled simulations to explore the full range of variability imparted by these clouds and convective changes during the paleoclimate simulations. However, these coupled experiments are computationally expensive, taking months to years of a 'real time' to complete; they are thus beyond the scope of this proof-of-concept study (but are planned in the future). The practical consequence is that variability over the ocean, especially, is throttled, and the climate system during the paleoclimate runs may no longer be in radiative equilibrium (a symptom of the incomplete climate response to the strong paleoclimate forcing perturbed parameter runs); we note the net top of the atmosphere radiative balance of each simulation (Table 1).

The basic structure of the clouds and convection schemes are described in (Kim and Kang, 2012; Del Genio, 2012; Del Genio *et al.*, 2015). We have chosen here to explore six different parameters utilized in the cloud and convection schemes that likely have a substantive impact on ECS as well as water isotope distribution (Table 1). A total of 19 simulations were performed for each time period. Parameters chosen are ones not directly constrained by current in situ or satellite observing platforms, yet are commonly perturbed in GCM atmosphere tuning efforts (Hourdin *et al.*, 2017; Schmidt *et al.*, 2017).

Rain re-evaporation above the cloud base (*rev*) has been a parameter previously considered for change because it improves convection and variability (e.g., Madden-Julian Oscillation in (Kim and Kang, 2012)). This parameter makes the GISSE-2.2 model distinct from the GISSE-2.1 (Rind *et al.*, 2020). Water isotopes are sensitive to changing this parameter (Field *et al.*, 2014). Increasing this parameter results in additional atmospheric moistening and a subsequent increase in precipitation over the Maritime Continent (i.e., increased bias); however, it does typically improve isotopic matches between GISS-E2.1 simulations and satellite observations (Worden *et al.*, 2007).

The entrainment rate (*entr*) parameters control how much environmental mass is entrained into a less- and more-entraining convective plume. At most, two updraft plumes are permitted to initiate at each model level in the GISS convective scheme, and the only requirement is that they have different entrainment rates thus allowing a representation of shallow (i.e., more entraining) and deep (i.e., less entraining) convective towers within any convective cloud ensemble in the GCM grid box.

The convective adjustment time (*tconvadj*) is a parameter that controls how quickly convective mass reaches the tropopause, and thus how quickly the environmental profile of temperature and moisture adjusts to moist convective processes.

The convective trigger (*ctrigger*) parameter determines what environmental conditions are necessary for initiating convection. Physically this parameter can be interpreted as accounting for the multi-faceted role that the planetary boundary layer plays in convective initiation (e.g., turbulent lifting of parcels, variations in near-surface stability or moisture across a grid box), the role of vertical wind shear, the role of mesoscale ascent causing local destabilization, or the role of gravity waves in the weakening of convection-inhibiting stable layers.

The radius multiplier (*droprad*) is a parameter that governs the sizes of liquid droplets and ice particles for a given condensate amount. Though there are some observational estimates of sizes at cloud tops (Elsaesser *et al.*, 2017a, and references therein), within-cloud estimates are largely unconstrained (and particularly within convection, where attenuation of radiometric signals are substantial). In general, smaller sizes result in clouds reflecting more shortwave radiation coincident with reduced outgoing longwave radiation.

Auto-conversion of cloud water content to precipitation is governed by a critical cloud water content scaling parameter (*critQ*). Any liquid or ice water content above the scaled critical threshold will be converted to precipitation via auto-conversion, thus affecting cloud condensate, cloud fractions, and in turn, radiation.

2.4 Satellite data

Our perturbed parameter configurations are evaluated using multiple present-day satellite climatologies provided by the Obs4MIPS project (https://esgf-node.llnl.gov/projects/obs4mips/) hosted on the Earth System Grid Federation (https://esgf.llnl.gov). Top of the atmosphere absorbed shortwave (SWabsTOA) and outgoing longwave radiation (OLR), along with cloud radiative forcing estimates (SW_CRE, and LW_CRE) are provided by the CERES EBAF Edition 4.1 product (Kato *et al.*, 2018; Loeb *et al.*, 2018, 2020). Temperature and water vapor profiles are provided by AIRS Version 6 retrievals (Tian *et al.*, 2019; Tian and Hearty, 2020) for altitudes at and below 600 hPa, and by MLS Version 4 satellite retrievals (Waters *et al.*, 2006) at and above 200 hPa. Column integrated total (cloud plus precipitating) liquid water estimates (TLWP) are provided by the MAC-LWP (Elsaesser *et al.*, 2017b) and TRMM 3A12 (Kummerow *et al.*, 2001) products, while the column integrated ice counterparts (TIWP) are provided by the CloudSat 2C-Ice (Deng *et al.*, 2015) R05 and MODIS C6 (Platnick *et al.*, 2015; Marchant *et al.*, 2016; Yi *et al.*, 2017) products. Total precipitation (prec) is provided by GPCP Version 2.3 (Adler *et al.*, 2003) and TRMM TMPA (Huffman *et al.*, 2007; Adler *et al.*, 2009) Version 7 products. Convective precipitation (prec_mc) is provided by the GPM Dual-frequency

Precipitation (DPR) Radar product (Iguchi *et al.*, 2012). Global total cloud cover (tcc_isccp) is provided by the ISCCP (Rossow and Schiffer, 1999) D1 total cloud fraction product, while surface wind estimates are provided by the QuikSCAT satellite and Remote Sensing Systems surface wind products (Wentz *et al.*, 2007; Wentz and Schabel, 2000).

We compared these multiple satellite climatologies to the perturbed parameter simulations and computed both global and proxy site-averaged root mean square error (RMSE) scores.

2.5 Paleoclimate data

To evaluate the atmosphere-only $\delta^{18}O_p$ simulations, we used land-based paleoclimate constraints which are less impacted by the lack of surface ocean and ice feedbacks in these runs, minimizing proxy-model mismatches that may be expected from including ice core records. We used the latest Speleothem Isotope Synthesis and Analysis (SISAL) version 2 database (Comas-Bru *et al.*, 2020) and extracted 378 speleothem records from a total of 224 unique sites. In this version, multiple age models for most cave sites were generated but we used the original published chronologies in obtaining mean $\delta^{18}O$ over the following time periods: LGM (21 ± 1 ka), MH (6 ± 1 ka) and PI (last 2 ka). Depending on the mineralogy (i.e., calcite or aragonite), mean $\delta^{18}O$ values (VPDB) were converted to their drip water equivalents analogous to $\delta^{18}O_p$ (VSMOW) (Comas-Bru *et al.*, 2019). We used model-generated mean annual SAT extracted at the grid points nearest the cave sites as representative for cave temperatures required in the drip water conversion. Records where mineralogy is unknown or mixed were excluded. Multiple records in a single site and model grid box were then averaged except for those that report large dating errors (e. g., Kesang Cave, (Cai *et al.*, 2017)). A total of 257, 195 and 81 records were obtained for the PI, MH and LGM periods, respectively.

2.6 Sensitivity to perturbations and proxy-model comparison

To assess the spatial sensitivity of $\delta^{18}O_p$ to perturbations in cloud and convective parameterizations, we derived z-scores for each experiment, $z = \frac{(x-\mu)}{\sigma}$; where x is the mean $\delta^{18}O_p$ of an ensemble member over two decades (see Section 2.2) , μ is the PPE mean and σ is the standard deviation about the mean decadal variability of each experiment per grid box. We counted the number of ensembles per grid box where the absolute value of the z-score is greater than 1 and then normalized the total against the number of PPE runs to derive a sensitivity score. A maximum score of 1 indicates that all 19 ensemble members show significant difference from the PPE mean, and thus the highest sensitivity to parameter changes. We similarly evaluated the spatial sensitivity of PREC and SAT to parameter changes.

Simulated $\delta^{18}O_p$ from the nearest grid points to the cave sites were compared with associated proxy values for each period; time slice anomalies for each period relative to PI were also examined. Skill statistics were calculated over each time period using a weighted least square regression and RMSE. The weights applied to the extracted grid points were the derived sensitivity scores of a $\delta^{18}O_p$ grid box to changes in cloud and convective parameterizations as discussed above, highlighting the strength of a proxy site in discriminating among perturbations (i.e., weight of 1) or penalizing a proxy site for exhibiting small changes with each perturbation (i.e., weight of 0).

3 Results

3.1 Spatial sensitivity to perturbations in clouds and convective parameterizations

Based on the resultant spatial variability of precipitation (PREC), surface air temperature (SAT), and $\delta^{18}O_p$ (Text S1 in the supporting information), we derived scores that represent the number of simulations in the ensemble per grid box showing significant difference from the PPE mean (see Section 2.6) to highlight spatial sensitivity to parameterization choices. Using the simulations from the balanced version, PREC and $\delta^{18}O_p$ are more sensitive to parameter changes, with over 30% of the overall land surface showing significant difference from the mean across all time periods (Figure 1). SAT, on the other hand, shows less sensitivity, covering less than 30% of the total land surface.

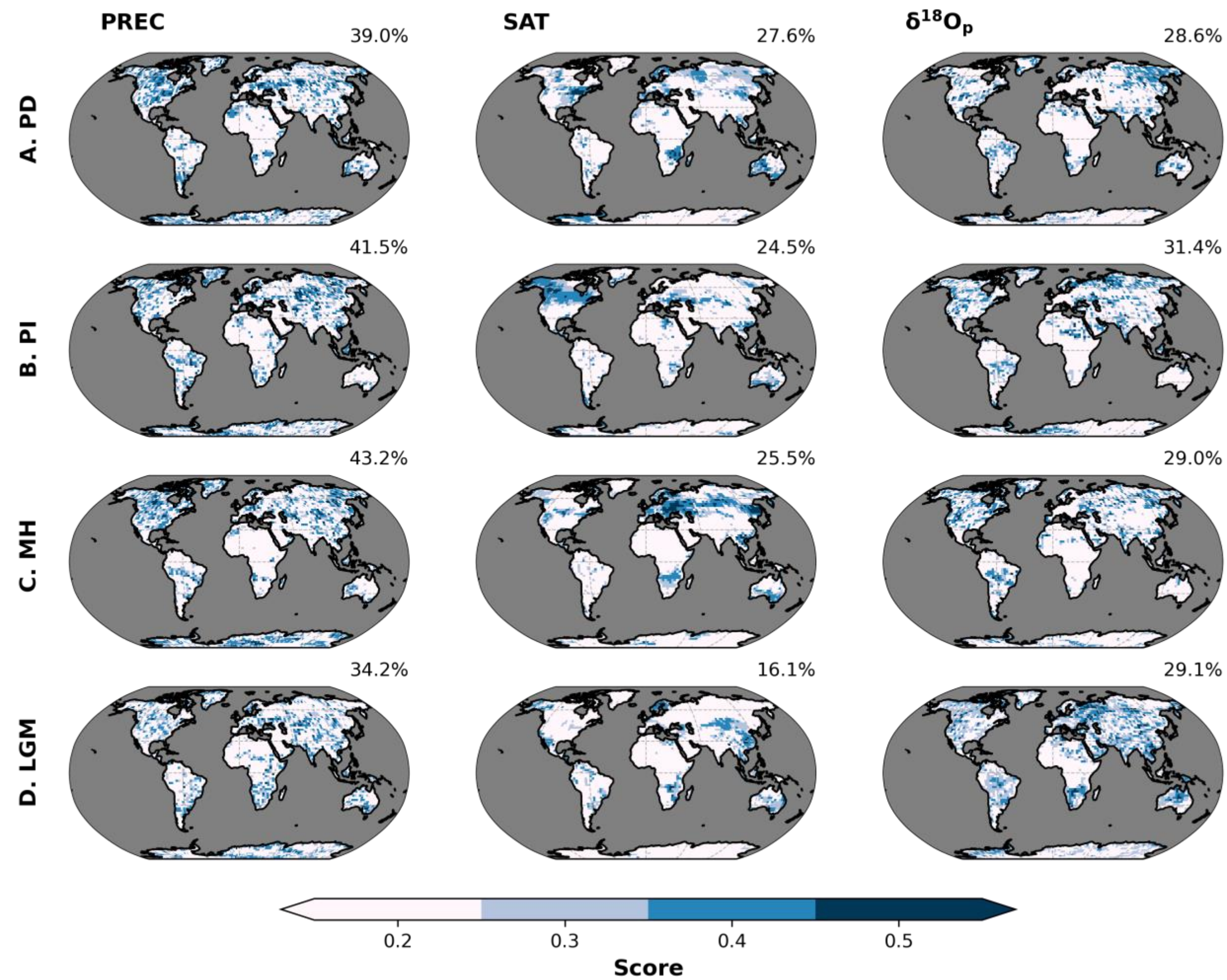

Figure. 1. Spatial patterns in sensitivity of precipitation (PREC), surface air temperature (SAT), and $\delta^{18}O_p$ to perturbed cloud and convective parameters for different time periods (a-d). Shading represents the scores or the fraction of the total number of ensembles per grid box showing significant difference from the PPE mean. The higher the score, the more sensitive a location is to parameter changes. The oceans are masked to highlight changes on land for these atmosphere-only simulations. Percentages reported at the top right of each panel indicate the fraction of land surface (using PD configuration in order to to facilitate comparison across time periods) having a score greater than 0.2.

The regions that are *most* sensitive to clouds and convective processes in the GISS-E2.1 simulations of SAT are spatially varying across time periods while that of PREC and $\delta^{18}O_p$ are located almost everywhere except for interior Africa (Figure 1). Based on our PPE simulations, these regions form the key sites to which model results may be principally constrained by the presence of viable paleo-proxy records.

Relative to the PI period, sensitive regions for each variable increase in extent in the MH and LGM periods (Figure 2), indicating that paleoclimate simulations are more sensitive to parameter changes relative to the modern. This supports the premise of this proof-of-concept study that paleoclimate simulations, especially that of $\delta^{18}O_p$ where parameter sensitive regions can be found almost everywhere, may be better at discriminating cloud and convective parameterization changes across multiple PPE members than modern.

This observation is consistent with that of the unbalanced version, however, the spatial extent or the fraction of land surface of highly parameter-sensitive sites has decreased across all time periods (Text S1, Figures S3 and S4 in the supporting information), indicating that without re-tuning, model sensitivity decreases.

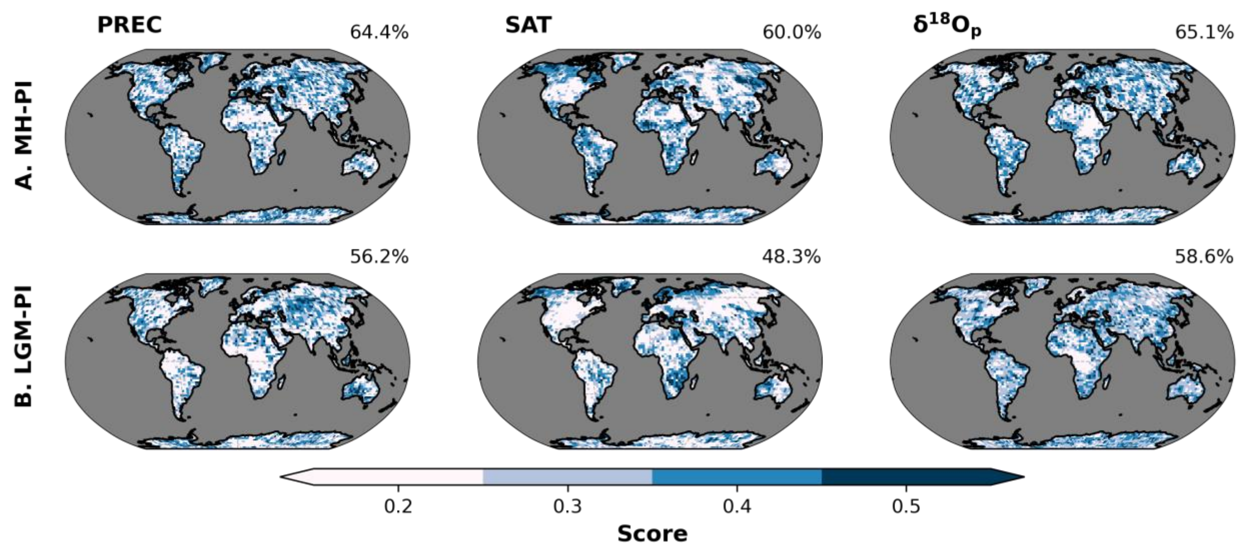

Figure 2. Same as Figure 1 but for (a) MH-PI and (b) LGM-PI anomalies.

3.2 Model evaluation using multiple satellite climatologies

Radiation, cloud, and thermodynamic variables from modern PPE simulations are compared to satellite estimates provided largely from the Obs4MIPS archive (Waliser *et al.*, 2020) (see Section 2). It is often the case that inter-product differences for any cloud or thermodynamic variable exceeds published random noise or uncertainty estimates. Such differences arise due to systematic regime-dependent unknowns in satellite cloud and precipitation remote sensing (Rapp *et al.*, 2009; Elsaesser and Kummerow, 2015; Liu *et al.*, 2017; Duncan and Eriksson, 2018). To avoid root mean square error (RMSE) scores being dependent on any one satellite product choice, we explicitly account for satellite product systematic biases by allowing no contribution to RMSE if the model field falls within the observational range bounded by the minimum and maximum product estimates.

RMSE derived for global, as well as for grid boxes co-located only with proxy sites, are shown in Figure 3. Across the board, RMSE is lower with a more muted response across PPE members for proxy site locations, where on average, both total and convective rainfall are a factor of ~2 less than the tropical (30°S-30°N) avearge. Less convection implies a smaller reliance on convective and cloud parameterizations, and a less complex atmosphere to simulate. Both *entr60-40* and *tconvadjX2* are slightly more skillful for proxy site PREC, with a 5-10% reduction in RMSE compared to *std*, the default mode for GISS-E2.1; *critQ1-0.5* was the configuration exhibiting subtle improvement across more diagnostics than other PPE members. When considering global scores, the top two performers change to *droprad50-50* and *trigger1.0,* with both exhibiting the lowest global RMSE for PREC. Interestingly, when considering convective precipitation (prec_mc) only, both *tconvadjX2* and *trigger0.99* outperform to a large degree, with both exhibiting a 10 to 20% reduction in RMSE (the *trigger0.99* result is opposite to what is inferred from the proxy-only site satellite score). Relative to the work of Field *et al.*, 2014, we have a smaller PD spread in δ^{18}O vapor. This change is likely due to the *rev* parameter being turned off in all of the Field *et al.*, 2014 experiments, and highlights the need to do multiple parameter changes simultaneously in future work to infer a more complete picture of sensitivity to parameters.

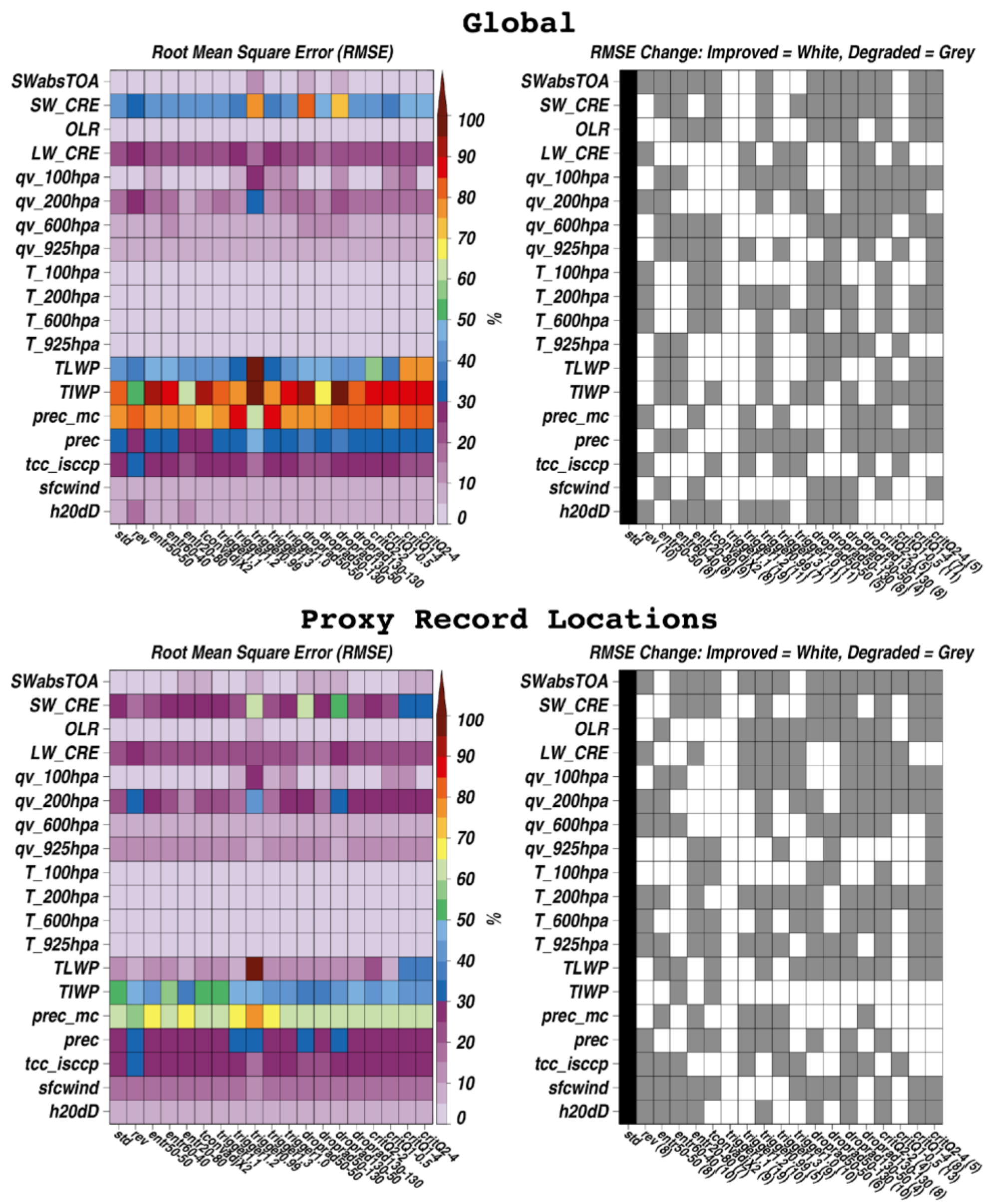

Figure 3. Comparison of model with satellite data. (top left) Global model-satellite RMSE scores for absorbed shortwave (SW) radiation at the top of the atmosphere (SWabsTOA), SW cloud radiative effects (SW_CRE), outgoing longwave radiation (OLR), longwave (LW)_CRE, water vapor (qv) and temperature (T) at various levels, total (cloud+precipitating) liquid and ice water paths (TLWP, TIWP), convective and total precipitation (prec_mc, prec), ISCCP satellite cloud cover (tcc_isccp), 10-meter surface wind speeds (sfcwind) and δD. (top right) binary white-gray shading indicating if RMSE scores improved for a given ensemble member relative to *std*, with numbers in parenthesis indicating the number of metrics exhibiting improvement.

(bottom row) As in the top row, but only for model and satellite grid boxes co-located with paleo-proxy sites.

3.3 Model evaluation using proxy data under PI, MH and LGM conditions

Our selected proxy database comprises a total of 257, 195 and 81 records for the PI, MH and LGM periods, respectively. From each of the models, we extracted the simulated $\delta^{18}O_p$ nearest each cave site. As shown in our proxy-model comparisons (Figure 4), the mean $\delta^{18}O_p$ distribution in all runs and time periods are in excellent agreement with the proxies. In these comparisons, we prescribed weights to the simulated $\delta^{18}O_p$, based on Figure 1, which gives importance to the spatial sensitivity of a particular site to parameter changes. Weighting to z scores (Figure 1) significantly improved the overall proxy-model agreement compared to the unweighted calculation (Figure S6-a to -s and S7 in the supporting information).

While these first order comparisons show excellent agreement, discrepancies remain; for example, simulated $\delta^{18}O_p$ is more negative (positive) at low (mid- to high) latitude speleothem sites compared to the proxies, with those from the LGM exhibiting the largest offsets (Figure 4). These discrepancies could be due to cave specific factors and model limitations (see Discussion) that may exacerbate proxy-model mismatches. Because simulated $\delta^{18}O_s$ has the potential to better reflect processes within the karst system, we then compared the proxies with the $\delta^{18}O_s$ model results. Comparisons show high and significant correlations across all time periods ($r^2_{\delta 18Os}$ > 0.85, Figure S8 and S9 in the supporting information) with the less depleted $\delta^{18}O_s$ values showing a better match than the more depleted $\delta^{18}O_s$ values. However, the mismatch between the more depleted $\delta^{18}O_s$ values remain, leading to an overall lower agreement compared with using the simulated $\delta^{18}O_p$ results ($r^2_{\delta 18Op}$ > 0.87, Figure S9 in the supporting information). Average transit times from the surface to the cave systems over multiple years, along with site-specific karstic groundwater mixing effects, varies from each cave site, and thus may not be fully represented in the models especially at individual speleothem sites exhibiting strong annual or seasonal signals (e.g., (Comas-Bru *et al.*, 2019)).

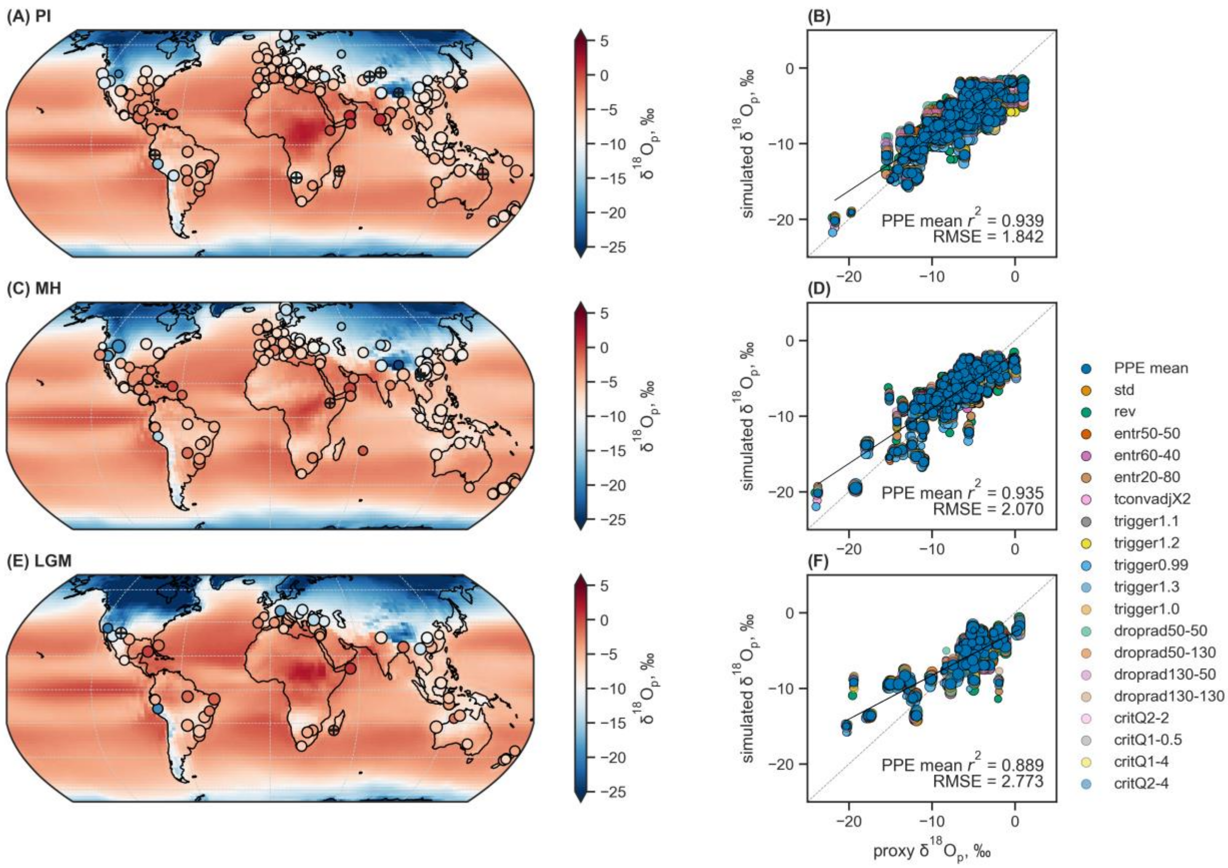

Figure 4. Comparison of simulated $\delta^{18}O_p$ with speleothem $\delta^{18}O$. Global distribution of simulated $\delta^{18}O_p$ (background) and speleothem $\delta^{18}O$, converted to their drip water equivalents (See Materials and Methods) under (a) PI (*n* = 257), (c) MH (*n* = 195) and (e) LGM (*n* = 81) conditions. Background and extracted data points are from the PPE mean. SISAL $\delta^{18}O$ points with standard deviation greater than 1 are marked with '+'. Scatterplots between simulated and proxy $\delta^{18}O_p$ for the respective time periods (b, d, f). PPE members are differentiated by color. Black lines represent the weighted least squares regression fits to data points while the gray dashed lines represent the 1:1 line. Weighted r^2 and RMSE for the PPE mean are reported in the lower right corner of each scatterplot. The size of the circles in all plots are scaled to the sensitivity scores derived in Figure 1. Results for each ensemble member are in Figure S6-a to S6-s in the supporting information.

Spread among the weighted r^2 values in each simulation is small (standard deviation, $\sigma <$ 0.05, Figure 5), indicating that the parameterization choices do not drastically impact $\delta^{18}O_p$

simulations, consistent with the proxy site-collocated satellite results. Nonetheless, certain simulations show higher r^2 values than that of the *std* run, representing an improvement in the level of agreement between models and proxies. The critical cloud water content (*critQ1-4*), entrainment rate for plume (*entr50-50*) and convective trigger (*trigger0.99*) parameters exhibit the highest skill for the PI (r^2 = 0.944, RMSE = 1.794‰), MH (r^2 = 0.940, RMSE = 2.007‰) and LGM (r^2 = 0.897, RMSE = 2.673‰) periods, respectively. Considering only the sites common across the time periods (i.e., limited by the number of LGM sites), the *entr60-40* and *tconvadjX2* parameters emerged as the best performing simulation for the PI (r^2 = 0.940, RMSE = 1.855‰) and MH (r^2 = 0.940, RMSE = 1.710‰), respectively, indicating that the reduced number and spatial spread of data points, with the influence of weighting, impacts model performance. These results, broadly consistent with some of the best performers derived from satellite comparisons (considering only the proxy sites), suggest that while different cloud and convective scheme settings do not necessarily impose large changes on the model results for the sites considered, the *best* parameterization for each time period may vary likely depending upon the prevailing boundary condition. This warrants further investigation involving the use of the more appropriate fully-coupled simulations using these parameterizations.

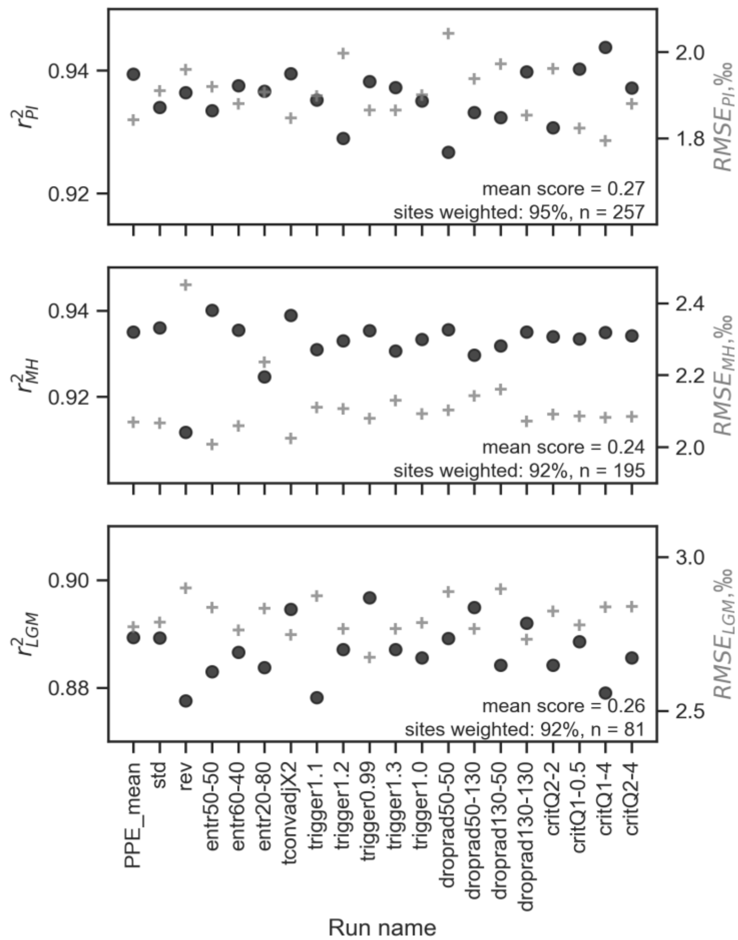

Figure 5. Weighted r^2 (black dots) and RMSE (gray crosses) values between simulated $\delta^{18}O_p$ and SISAL $\delta^{18}O$ for all time periods. All speleothem $\delta^{18}O$ were converted to their drip water equivalent.

3.4 LGM and MH isotopic changes and model performance

To investigate the impact of parameter changes on the relative shift in $\delta^{18}O_p$, we computed anomalies between the LGM and MH relative to the PI. LGM-PI anomalies consist of 17 records whereas MH-PI anomalies contain 79 records. Similar to the absolute value comparisons, we prescribed weights (extracted from Figure 2) to the simulated $\delta^{18}O_p$ anomalies. The spatial distribution of simulated LGM-PI $\delta^{18}O_p$ in the PPE mean shows an overall depletion over land, with the northern latitudes (i.e., ice sheet over North America and Europe) exhibiting the greatest negative $\delta^{18}O_p$ excursions – a direct consequence of temperature-dependent fractionation at higher latitudes (Figure 6A). In contrast, the mid-latitudes are only slightly depleted while the Amazon, northern Africa, Himalayas, and oceanic regions show overall positive $\delta^{18}O_p$ anomalies, consistent with the overall drier/cooler conditions during the LGM relative to present.

Comparison with SISAL $\delta^{18}O$ anomalies show moderate and statistically significant ($p < 0.005$) proxy-model relationship (Figure 6B, Figure 7) with at least 70% of the records sharing similar signs. The strong positive and negative anomalies observed in Paraiso cave, Brazil, and Sofular cave, Turkey, respectively, are not captured by the models, where simulated $\delta^{18}O_p$ changes instead show values closer to zero. The spread among the weighted r^2 values remains small ($\sigma < 0.06$, Figure 7). The *rev* parameterization outperformed the *std* run, exhibiting the lowest proxy-model mismatch compared to other parameterization results ($r^2 = 0.647$, RMSE = 1.152‰, Figure 7). Regions of notable model improvement are in the Maritime Continent (n = 4), Africa (n = 2) and the Middle East (except Sofular cave, n = 2) showing a 55%, 34% and 32% mean decrease in error relative to the *std*, respectively.

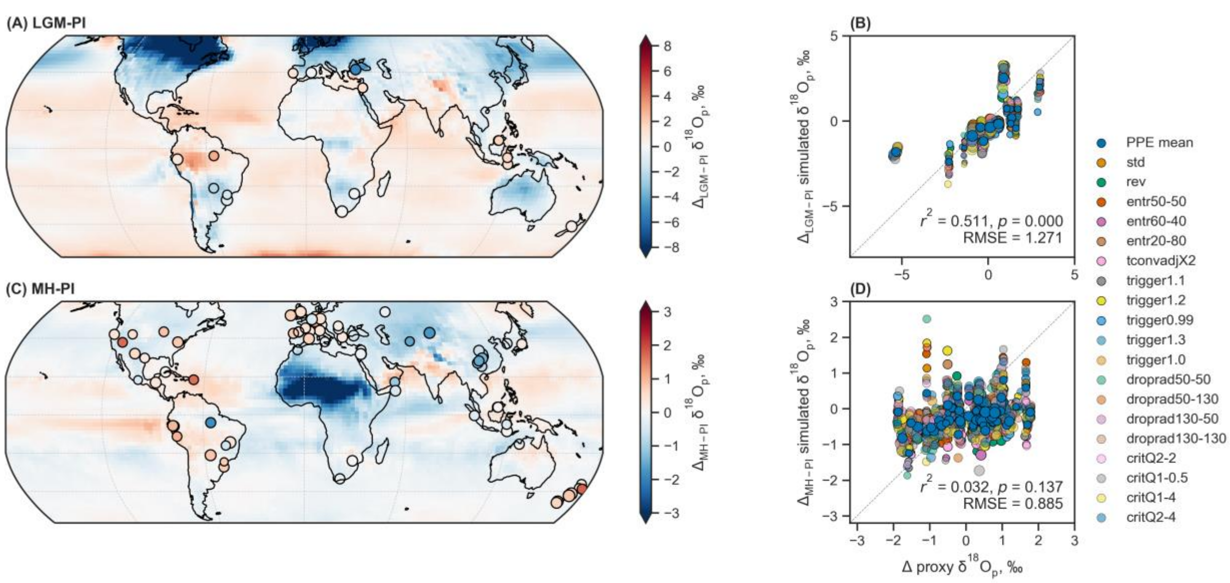

Figure 6. Comparison of simulated $\delta^{18}O_p$ anomalies (background) with speleothem $\delta^{18}O$ (filled circles) for each time slices: (a) LGM-PI (n = 17), (c) MH-PI (n = 79). Background and extracted

data points are from the PPE mean. Scatterplots between simulated and proxy $\delta^{18}O_p$ for the respective time periods (b, d). PPE members are differentiated by color. Gray dashed lines represent the 1:1 line. Weighted r^2 and RMSE for the PPE mean are reported in the lower right corner of each scatterplot. The size of the circles in all plots are scaled to the sensitivity scores derived in Figure 2. Results for each ensemble member are in Figure S10-a to S10-s in the supporting information.

Compared to LGM variations, MH changes relative to PI are more modest. Interior South America, India and northern Australia show positive $\delta^{18}O_p$ anomalies in the PPE mean (Figure 6C). In contrast, North America, Eurasia, Himalayas, and East Asia show negative $\delta^{18}O_p$ anomalies, with the western and central African region showing the greatest negative $\delta^{18}O_p$ excursions – a consequence of simulated decrease in surface temperature and increased precipitation or monsoon over these regions. Proxy-model agreement across runs lack skill in replicating MH-PI isotopic changes observed in the SISAL records (Figure 6D, 7), with only 35% of the records showing similar signs in the PPE mean. The largest deviations are found in North and Central America (South America) where positive (negative) anomalies are not reflected in the simulated $\delta^{18}O_p$ changes. Overall, the magnitude of change is consistently smaller in the simulations (Figure 6D), as similarly observed in other models using fully coupled simulations (e.g., (Cauquoin *et al.*, 2019; Comas-Bru *et al.*, 2019)). Of the 19 PPE members, only 4 show statistically significant ($p < 0.04$) relationship with the proxies, outperforming the *std* $\delta^{18}O_p$ run (Figure 7). The best performing parameterization is *critQ2-4* (weighted r^2 = 0.129, RMSE = 0.843‰, Figure 7), where 44% of the data points now share similar signs. Notable regions of observed model improvement are in North America (n = 6) and Europe (n = 14) showing a 14% and 30% mean decrease in error relative to the *std*, respectively. Reducing the number of datapoints to match the sites from the LGM-PI changes shows a different result such that the *trigger1.0* parameterization now shows the highest skill (weighted r^2 = 0.228, RMSE = 0.886‰).

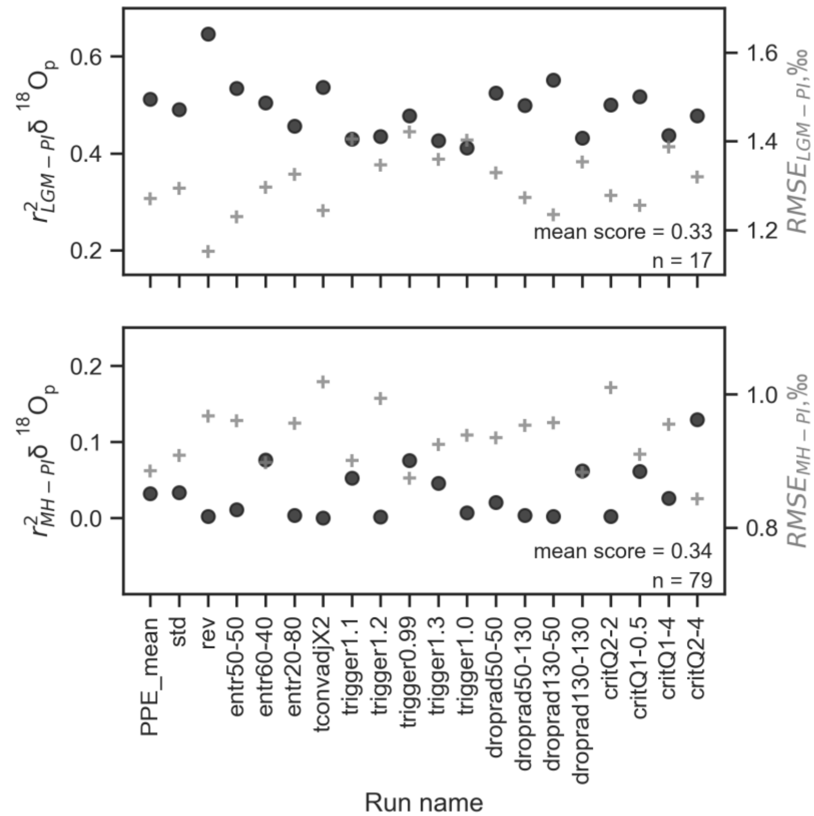

Figure 7. Weighted r^2 (black dots) and RMSE (gray crosses) values between simulated $\delta^{18}O_p$ and SISAL $\delta^{18}O$ anomalies for LGM-PI (top) and MH-PI (bottom).

4 Discussion and Conclusions

In this study, we have identified parts of the world that are most sensitive to convective and cloud parameterizations, which may provide the best opportunity for constraining key metrics in climate models. These areas could potentially be the target locations for developing other proxy climate archives if the results of our GISS E2.1 simulations are held up across other models. Parameter-sensitive sites are different between the balanced and unbalanced versions of the models with the latter showing more regions of lower sensitivity scores. This is likely related to the greater variability among PPE members induced by changes in the spatial extent of mean

SAT, PREC and $\delta^{18}O_p$ by the parameter perturbations (Figure S1 and S2 in the supporting information), affecting more indiscriminate regions in the world. This outcome from the unbalanced version is less useful in constraining biases related to cloud and convective parameterizations.

Our satellite-model analyses, stratified by global and proxy-specific skill scores, reveal that the distribution of proxy sites here lie outside of the spatial domains most impacted by cloud and convective parameterization choices. This suggests a need for additional optimally suited sites distributed across more complex convection-cloud schemes (e.g., tropical oceans) to constrain global simulations. Additionally, determining convective- and parameter-sensitive areas across the world using different coupled atmosphere-ocean-vegetation models could provide an excellent framework for targeted paleoclimate fieldwork to develop new archives and records.

Though the proxy sites are located in less complex atmospheric scenes (e.g., Africa where the biggest MH-PI contrast occurs lack speleothem records as a function of geology), the first order spatial pattern of $\delta^{18}O_p$ is in excellent agreement between proxy data and all PPE members across all time periods. Also partly supported by the satellite analyses, three parameterizations with highest model skill emerged: a 1:4 liquid and ice split for critical cloud water content (*critQ1-4*) for the PI period, a 50:50 split of entrainment rate for plume (*entr50-50*) for the MH and convective trigger of 0.99 (*trigger0.99*) for the LGM period. The simulations are able to capture broad scale LGM-PI $\delta^{18}O_p$ patterns where the *rev* parameterization performed best among PPE members. On the other hand, model skill is significantly reduced in the MH-PI runs where the magnitude of change is consistently smaller in all simulations compared to the proxies. Nonetheless, *critQ2-4* parameterization outperformed the *std* in the MH-PI simulations.

Differences in the prevalence and average depth of convection across these warmer and cooler periods would indeed suggest that different parameters (which correspond to different aspects of convection) are more impactful on time period-dependent skill. These time period-dependent results motivate the need to perturb numerous parameters simultaneously toward determining if optimal multi-parameter vectors exist across all periods.

It is highly likely that the coupled simulations of these same experiments will exhibit a greater range of variability across simulations. The fixed SSTs in our runs allowed us the ability to explore this approach with computationally inexpensive simulations; however, it also throttles coupled feedbacks muting LGM and MH variability across ensemble members and precluded us from calculating ECS for every perturbed parameter. Further, these fixed surface ocean conditions limit the paleoclimate constraints to land-based proxy archives. Other potential sources of model discrepancies are related to ice sheet topography changes and dust concentrations (LGM), along with the lack of vegetation and dust concentration feedbacks (LGM and MH) (Crucifix and Hewitt, 2005; Masson-Delmotte *et al.*, 2006; Harrison *et al.*, 2014; Ullman *et al.*, 2014), which may be best evaluated using fully coupled atmosphere-ocean models.

Speleothem proxy climate records have their own set of uncertainties. Speleothem $\delta^{18}O$ primarily reflects local and regional climate signals controlling $\delta^{18}O_p$. However, this signal may be altered as it enters the soil zone and epikarst, a zone that stores infiltrated rainwater, through mixing with existing waters, seasonality of recharge rates, and fractionation by evaporation before reaching the cave system (Hartmann and Baker, 2017; Baker *et al.*, 2019). Within the cave itself, the calcite $\delta^{18}O$ signal can be further altered by non-equilibrium fractionation processes and temperature-dependent fractionation during speleothem deposition (Lachniet, 2009; Hartmann and Baker, 2017; Baker *et al.*, 2019). Using $\delta^{18}O_s$ instead of $\delta^{18}O_p$ in the comparisons did not show an improvement either (Figure S8, S9 in the supporting information). These cave specific factors are not reproduced in the models, exacerbating discrepancies between proxies and simulations. Converting speleothem $\delta^{18}O$ to its drip water equivalent similarly introduces uncertainties as past cave temperatures are unknown (Comas-Bru *et al.*, 2019). A natural next step to better comparing the models to proxies is to convert the model output into proxy space via proxy system models, an area of ongoing research (Evans *et al.*, 2013; Dee *et al.*, 2017).

While model biases and proxy uncertainties remain, our initial results add to the growing body of work that demonstrates the utility of paleoclimate data in better constraining model skill, particularly at the model development stage (Tierney *et al.*, 2020a, 2020b; Zhu *et al.*, 2021). Our approach and results may be extended to other GCMs and could be especially useful for other models using similar parameters in their cloud and convective parameterizations. Because cloud feedbacks within the climate system are non-stationary under varying boundary conditions (Zhu *et al.*, 2019), hence leading to differences in which parameterization experiment performs best for each time period, this further supports the proposition that fine-tuning future simulations requires determining all plausible parameter combinations and testing the limits of parameter values used in this study. Future work applying this framework to coupled ocean-atmosphere simulations and incorporating vegetation and dust change is needed to fully investigate the impact of parameter choices on paleoclimate simulations. Incorporation of other land-based water isotope proxies such as those from ice cores, and inclusion of SST proxies which reflects expected changes in radiative balance, will allow for further model evaluation. Techniques like paleoclimate data assimilation could also be leveraged to identify optimal parameter choices that best matches the paleorecord, and subsequently better constrain ECS as previously demonstrated (Annan *et al.*, 2013; Hargreaves and Annan, 2002; Osman *et al.*, 2021; Tierney *et al.*, 2020a).

Acknowledgments

We thank three anonymous reviewers for their helpful comments that improved the manuscript. We thank NASA GISS and the NASA Center for Climate Simulation for institutional support. The satellite data aggregation and analysis contributions by GSE are supported by the NASA Data for Operations and Assessments (NDOA) program (Grant #NNX17AF46G), the Science of Terra, Aqua and Suomi NPP Program (Grant #80NSSC18K1030), and the Precipitation Measurement Missions (PMM) program (Grant #80NSSC22K0609). This study was supported by a National Science Foundation Paleo Perspectives on Climate Change (P2C2) Award (Award Number 1805544) to Michael Griffiths.

Open Research

Our perturbed parameter configurations were evaluated using multiple present-day satellite climatologies provided by the Obs4MIPS project (https://esgf-node.llnl.gov/projects/obs4mips/) hosted on the Earth System Grid Federation (https://esgf.llnl.gov/). Top of the atmosphere absorbed shortwave (SWabsTOA) and outgoing longwave radiation (OLR), along with cloud radiative forcing estimates (SW_CRE, and LW_CRE) are provided by the CERES EBAF Edition 4.1 product (Kato *et al.*, 2018; Loeb *et al.*, 2018, 2020). Temperature and water vapor profiles are provided by AIRS Version 6 retrievals (Tian *et al.*, 2019; Tian and Hearty, 2020) for altitudes at and below 600 hPa, and by MLS Version 4 satellite retrievals (Waters *et al.*, 2006) at and above 200 hPa. Column integrated total (cloud plus precipitating) liquid water estimates (TLWP) are provided by the MAC-LWP (Elsaesser *et al.*, 2017b) and TRMM 3A12 (Kummerow *et al.*, 2001) products, while the column integrated ice counterparts (TIWP) are provided by the CloudSat 2C-Ice (Deng *et al.*, 2015) R05 and MODIS C6 (Marchant *et al.*, 2016; Platnick *et al.*, 2015; Yi *et al.*, 2017) products. Total precipitation (prec) is provided by GPCP Version 2.3 (Adler *et al.*, 2003) and TRMM TMPA (Adler *et al.*, 2009; Huffman *et al.*, 2007) Version 7 products. Convective precipitation (prec_mc) is provided by the GPM Dual-frequency Precipitation (DPR) Radar product (Iguchi *et al.*, 2012). Global total cloud cover (tcc_isccp) is provided by the ISCCP (Rossow and Schiffer, 1999) D1 total cloud fraction product, while surface wind estimates are provided by the QuikSCAT satellite and Remote Sensing Systems surface wind products (Wentz and Schabel, 2000; Wentz *et al.*, 2007). GISS E2.1 model outputs for SAT, PREC, $\delta^{18}O_p$ and $\delta^{18}O_s$ for each simulation and time slice are uploaded in the nccs.nasa.gov data portal. The water isotope proxies were derived from the Speleothem Isotope Synthesis and Analysis (SISAL) version 2 database ((Comas-Bru *et al.*, 2020)) and can be accessed through https://researchdata.reading.ac.uk/256/.

References

Abe-Ouchi, A. et al. (2013), Insolation-driven 100,000-year glacial cycles and hysteresis of ice-sheet volume, *Nature*, *500*190-193, doi:10.7916/D8MC994B/download.

Adkins, J. F., and Schrag, D. P. (2003), Reconstructing Last Glacial Maximum bottom water salinities from deep-sea sediment pore fluid profiles, *Earth and Planetary Science Letters*, *216*(1-2), 109-123, doi:10.1016/S0012-821X(03)00502-8.

Adler, R. F. et al. (2003), The Version-2 Global Precipitation Climatology Project (GPCP) Monthly Precipitation Analysis (1979-Present), *Journal of Hydrometeorology*, *4*1147-1167.

Adler, R. F., Wang, J. J., Gu, G., and Huffman, G. J. (2009), A ten-year tropical rainfall climatology based on a composite of TRMM products, *Journal of the Meteorological Society of Japan*, *87A*281-293.

Annan, J. D., Crucifix, M., Edwards, T. L., and Paul, A. (2013), Parameter estimation using paleodata assimilation, in *PAGES news Vol 21(2)*, edited by P. Braconnot, C. Brierley, H. SP, L. von Gunten, and T. Kiefer, pp. 78-79, Bern, Switzerland.

Atsawawaranunt, K. et al. (2018), The SISAL database: a global resource to document oxygen and carbon isotope records from speleothems, *Earth System Science Data*, *10*1687-1713.

Baker, A. et al. (2019), Global analysis reveals climatic controls on the oxygen isotope composition of cave drip water, *Nature Communications*, *10*(2984), 1-7.

Berger, A., and Loutre, M. F. (1991), Insolation values for the climate of the last 10 million years, *Quaternary Science Reviews*, *10*(4), 297-317, doi:10.1016/0277-3791(91)90033-Q.

Bolot, M., Legras, B., and Moyer, E. J. (2013), Modeling and interpreting the isotopic composition of water vapor in convective updrafts, *Atmospheric Chemistry and Physics*, *13*7903-7935.

Bony, S., Risi, C., and Vimeux, F. (2008), Influence of convective processes on the isotopic composition (d18O and dD) of precipitation and water vapor in the tropics:1. Radiative-convective equilibrium and Tropical Ocean–GlobalAtmosphere–Coupled Ocean-Atmosphere ResponseExperiment (TOGA-COARE) simulations, *Journal of Geophysical Research, 113*D19305.

Boucher, O. et al. (2013), Clouds and Aerosols, in *Climate Change 2013: The Physical Science Basis. Contribution of Working Group I to the Fifth Assessment Report of the Intergovernmental Panel on Climate Change*, pp. 571-657, Cambridge University Press.

Brierley, C. M. et al. (2020), Large-scale features and evaluation of the PMIP4-CMIP6 midHolocene simulations, *Climate of the Past Discussions*, *16*(5), 1847-1872.

Briggs, R. D., Pollard, D., and Tarasov, L. (2014), A data-constrained large ensemble analysis of Antarctic evolution since the Eemian, *Quaternary Science Reviews*, *103*91-115.

Cai, Y. et al. (2017), Holocene moisture changes in western China, Central Asia, inferred from stalagmites, *Quaternary Science Reviews*, *158*15-28.

Caley, T., Roche, D. M., Waelbroeck, C., and Michel, E. (2014), Oxygen stable isotopes during the Last Glacial Maximum climate: perspectives from data-model (iLOVECLIM) comparison, *Climate of the Past*, *10*1939-1955.

Cauquoin, A., Werner, M., and Lohmann, G. (2019), Water isotopes-climate relationships for the mid-Holocene and preindustrial period simulated with an isotope-enabled version of MPI-ESM, *Climate of the Past*, *15*1913-1937.

Collins, M. et al. (2011), Climate model errors, feedbacks and forcings: a comparison of perturbed physics and multi-model ensembles, *Climate Dynamics*, *36*1737-1766.

Comas-Bru, L. et al. (2020), SISALv2: A comprehensive speleothem isotope database with multiple age-depth models, *Earth System Science Data*, *12*2579-2606.

Comas-Bru, L. et al. (2019), Evaluating model outputs using integrated global speleothem records of climate change since the last glacial, *Climate of the Past*, *15*1157-1579.

Crucifix, M., and Hewitt, C. D. (2005), Impact of vegetation changes on the dynamics of the atmosphere at the Last Glacial Maximum, *Climate Dynamics*, *25*(5), 447-459.

Dansgaard, W. (1964), Stable isotopes in precipitation, *Tellus*, *16*(4), 436-468.

Dee, S. G. et al. (2017), Improved spectral comparisons of paleoclimate models and observations via proxy system modeling: Implications for multi-decadal variability, *Earth and Planetary Science Letters*, *476*34-46.

Del Genio, A. D. (2012), Representing the sensitivity of convective cloud systems to tropospheric humidity in general circulation models, *Surveys in Geophysics*, *33*637-656.

Del Genio, A. D. et al. (2015), Constraints on Cumulus Parameterization from Simulations of Observed MJO Events, *Journal of Climate*, *28*(16), 6419-6442, doi:10.1175/JCLI-D-11-00168.1.

Deng, M., Mace, G. G., Wang, Z., and Berry, E. (2015), CloudSat 2C-ICE product update with a new Ze parameterization in lidar-only region, *Journal of Geophysical Research: Atmosphere*, *120*(23), 12198-12208, doi:10.1002/2015JD023600.

Dufresne, J.-L., and Bony, S. (2008), An assessment of the primary sources of spread of global warming estimates from coupled atmosphere-ocean models, *Journal of Climate*, *21*5135-5144.

Duncan, D. I., and Eriksson, P. (2018), An update on global atmospheric ice estimates from satellite observations and reanalyses, *Atmospheric Chemistry and Physics*.

Elsaesser, G. S., Del Genio, A. D., Jiang, J. H., and van Lier-Walqui, M. (2017a), An improved convective ice parameterization for the NASA GISS global climate model and impacts on cloud ice simulation, *Journal of Climate*, *30*(1), 317-336.

Elsaesser, G. S., and Kummerow, C. D. (2015), The sensitivity of rainfall estimation to error assumptions in a Bayesian passive microwave retrieval algorithm, *Journal of Applied Meteorology and Climatology*, *54*408-422.

Elsaesser, G. S. et al. (2017b), The Multisensor Advanced Climatology of Liquid Water Path (MAC-LWP), *Journal of Climate*, *30*10193-10210.

Evans, M. N., Tolwinski-Ward, S. E., Thompson, D. M., and Anchukaitis, K. J. (2013), Applications of proxy system modeling in high resolution paleoclimatology, *Quaternary Science Reviews*, *76*16-28.

Eyring, V. et al. (2016), Overview of the Coupled Model Intercomparison Project Phase 6 (CMIP6) experimental design and organization, *Geoscientific Model Development*, *9*1937-1958.

Fairchild, I. J., and Baker, A. (2012), Introduction to speleothems and systems, in *Speleothem Science: From Process to Past Environments*, edited by R. Bradley, pp. 432, Wiley-Blackwell, UK.

Field, R. D. et al. (2014), Evaluating climate model performance in the tropics with retrievals of water isotopic composition from Aura TES, *Geophysical Research Letters*, *41*6030-6036.

Flato, G. et al. (2013), Evaluation of Climate Models, in *Climate Change 2013: The Physical Science Basis. Contribution of Working Group I to the Fifth Assessment Report of the Intergovernmental Panel on Climate Change*, edited by T. F. Stocker et al., Cambridge University Press, Cambridge, United Kingdom and New York, NY, USA.

Frankenberg, C. et al. (2009), Dynamic processes governing lower-tropospheric HDO/H2O ratios as observed from space and ground, *Science*, *325*(5946), 1374-1377.

Galewsky, J. et al. (2016), Stable isotopes in atmospheric water vapor and applications to the hydrologic cycle, *Reviews of Geophysics*, *54*809-865.

Gat, J. R. (1996), Oxygen and Hydrogen Isotopes in the Hydrologic Cycle, *Ann Rev Earth Planet Sci*, *24*225-262.

Hargreaves, J. A., and Annan, J. D. (2002), Assimilation of paleo-data in a simple Earth system model, *Climate Dynamics*, *19*371-381.

Harrison, S. P. et al. (2014), Climate model benchmarking with glacial and mid-Holocene climates, *Climate Dynamics*, *43*671-688.

Hartmann, A., and Baker, A. (2017), Modelling karst vadose zone hydrology and its relevance for paleoclimate reconstruction, *Earth Science Reviews*, *172*178-192.

Hausfather, Z., Marvel, K., Schmidt, G. A., Nielsen-Gammon, J. W., and Zelinka, M. D. (2022), Climate simulations: recognize the ‘hot model’problem, *Nature*, *605*26-29.

Hourdin, F. et al. (2017), The art and science of climate model tuning, *Bulletin of the American Meteorological Society*, *98*(3), 589-602.

Huffman, G. J., Bolvin, D. T., Nelkin, E. J., Wolff, D. B., and Adler, R. F. (2007), The TRMM Multisatellite Precipitation Analysis (TMPA): Quasi-global, multiyear, combined-sensor precipitation estimates at fine scales, *Journal of Hydrometeorology*, *8*(1), 38-55.

Iguchi, T. et al. (2012), An overview of the precipitation retrieval algorithm for the Dual frequency Precipitation Radar (DPR) on the Global Precipitation Measurement (GPM) mission’s core satellite, *Proc. SPIE 8528, Earth Observing Missions and Sensors: Development, Implementation, and Characterization II*, *8528*85281C.

Indermühle, A. et al. (1999), Holocene carbon-cycle dynamics based on CO2 trapped in ice at Taylor Dome, Antarctica, *Nature*, *398*121-126.

IPCC (2021), Summary for Policymakers, in *Climate Change 2021: The Physical Science Basis. Contribution of Working Group I to the Sixth Assessment Report of the Intergovernmental Panel on Climate Change*, edited by V. Masson-Delmotte et al., Cambridge University Press, Kageyama, M. et al. (2021), The PMIP4-CMIP6 Last Glacial Maximum experiments: preliminary results and comparison with the PMIP3-CMIP5 simulations, *Climate of the Past*, *17*1065-1089.

Kageyama, M. et al. (2017), The PMIP4 contribution to CMIP6 – Part 4: Scientific objectives and experimental design of the PMIP4-CMIP6 Last Glacial Maximum experiments and PMIP4 sensitivity experiments, *Geoscientific Model Development*, *10*(11), 4035-4055, doi:10.5194/gmd-10-4035-2017.

Kato, S. et al. (2018), Surface Irradiances of Edition 4.0 Clouds and the Earth's Radiant Energy System (CERES) Energy Balanced and Filled (EBAF) Data Product, *Journal of Climate*, *31*(11), 4501-4527.

Kelley, M. et al. (2020), GISS-E2. 1: Configurations and climatology, *Journal of Advances in Modeling Earth Systems*, *12*(8), e2019MS002025.

Kim, D., and Kang, I. S. (2012), A bulk mass flux convection scheme for climate model: Description and moisture sensitivity, *Climate Dynamics*, *38*411-429.

Knutti, R., Rugenstein, M. A. A., and Hegerl, G. C. (2017), Beyond equilibrium climate sensitivity, *Nature Geoscience*, *10*727-736.

Kummerow, C. et al. (2001), The Evolution of the Goddard Profiling Algorithm (GPROF) for Rainfall Estimation from Passive Microwave Sensors, *Journal of Applied Meteorology*, *40*1801-1820.

Lachniet, M. (2009), Climatic and environmental controls on speleothem oxygen-isotope values, *Quaternary Science Reviews*, *28*412-432.

Lee, J.-E., Pierrehumbert, R., Swann, A., and Lintner, B. R. (2009), Sensitivity of stable water isotopic values to convective parameterization schemes, *Geophysical Research Letters*, *36*L23801.

LeGrande, A. N., and Schmidt, G. A. (2009), Sources of Holocene variability of oxygen isotopes in paleoclimate archives, *Climate of the Past*, *5*441-455.

Licciardi, J. M., Clark, P. U., Jenson, J. W., and DR, M. (1998), Deglaciation of a soft-bedded Laurentide Ice Sheet, *Quaternary Science Reviews*, *17*(4-5), 427-448.

Licciardi, J. M., Teller, J. T., and Clark, P. U. (1999), Freshwater routing by the Laurentide Ice Sheet during the last deglaciation, *Geophysical Monograph-American Geophysical Union*, *112*177-202.

Liu, J., Kummerow, C. D., and Elsaesser, G. S. (2017), Identifying and analysing uncertainty structures in the TRMM microwave imager precipitation product over tropical ocean basins, *International Journal of Remote Sensing*, *38*(1), 23-42.

Loeb, N. G. et al. (2018), Clouds and the Earth's Radiant Energy System (CERES) Energy Balanced and Filled (EBAF) Top-of-Atmosphere (TOA) Edition-4.0 Data Product, *Journal of Climate*, *31*895-918.

Loeb, N. G. et al. (2020), Toward a Consistent Definition between Satellite and Model Clear-Sky Radiative Fluxes, *Journal of Climate*, *33*61-75, doi:10.1175/jcli-d-19-0381.

Lopez, P. (2007), Cloud and precipitation parameterizations in modeling and variational data assimilation: A review, *Journal of the Atmospheric Sciences*, *64*(11), 3766-3784.

Marchant, B., Platnick, S., Meyer, K., Thomas Arnold, G., and Riedi, J. (2016), MODIS Collection 6 shortwave-derived cloud phase classification algorithm and comparisons with CALIOP, *Atmospheric Measurement Techniques*, *9*1587-1599.

Masson-Delmotte, V. et al. (2006), Past and future polar amplification of climate change: climate model inter comparisons and ice core constraints, *Climate Dynamics*, *26*513-529.

Mauritsen, T. et al. (2012), Tuning the climate of a global model, *Journal of Advances in Modeling Earth Systems*, *4*M00A01.

Meehl, G. A. et al. (2020), Context for interpreting equilibrium climate sensitivity and transient climate response from the CMIP6 Earth system models, *Science Advances*, *6*(26), eaba1981.

Noone, D. (2008), The influence of midlatitude and tropical overturning circulation on the isotopic composition of atmospheric water vapor and Antarctic precipitation, *Journal of Geophysical Research*, *113*D04102.

Nusbaumer, J., Wong, T. E., Bardeen, C., and Noone, D. (2017), Evaluating hydrological processes in the Community Atmosphere Model Version 5 (CAM5) using stable isotope ratios of water, *Journal of Advances in Modelling Earth Systems*, *9*949-977.

Osman, M. B. et al. (2021), Globally resolved surface temperatures since the Last Glacial Maximum, *Nature*, *599*(7884), 239-244.

Otto-Bliesner, B. L. et al. (2017), The PMIP4 contribution to CMIP6 – Part 2: Two interglacials, scientific objective and experimental design for Holocene and Last Interglacial simulations, *Geoscientific Model Development*, *10*(11), 3979-4003, doi:10.5194/gmd-10-3979-2017.

Peltier, W. R. (2004), Global glacial isostasy and the surface of the ice-age Earth: the ICE-5G (VM2) model and GRACE, *Annu. Rev. Earth Planet. Sci.*, *32*111-149.

Platnick, S. et al. (2015), MODIS cloud optical properties: User guide for the Collection 6 Level-2 MOD06/MYD06 product and associated Level-3 Datasets, 138.

Rapp, A. D., Elsaesser, G., and Kummerow, C. (2009), A combined multisensor optimal estimation retrieval algorithm for oceanic warm rain clouds, *Journal of Applied Meteorology and Climatology*, *48*(11), 2242-2256.

Ray, N., and Adams, J. (2001), A GIS-based vegetation map of the world at the Last Glacial Maximum (25,000-15,000 BP), *Internet Archaeology*, *11*1-44.

Rind, D. et al. (2020), GISS Model E2. 2: A climate model optimized for the middle atmosphere—Model structure, climatology, variability, and climate sensitivity, *Journal of Geophysical Research: Atmospheres*, *125*(10), e2019JD032204.

Risi, C. et al. (2012), Process-evaluation of tropospheric humidity simulated by general circulation models using water vapor isotopic observations: 2. Using isotopic diagnostics to understand the mid and upper tropospheric moist bias in the tropics and subtropics, *Journal of Geophysical Research*, *117*D05304.

Rossow, W. B., and Schiffer, R. A. (1999), Advances in Understanding Clouds from ISCCP, *Bulletin of the American Meteorological Society*, *80*(11), 2261-2288.

Schmidt, G. A. et al. (2014), Using paleo-climate comparisons to constrain future projections in CMIP5, *Climate of the Past*, *10*221-250.

Schmidt, G. A., Hoffman, D. L., Shindell, D. T., and Hu, Y. (2005), Modeling atmospheric stable water isotopes and the potential for constraining cloud processes and stratosphere-troposphere water exchange, *Journal of Geophysical Research*, *110*D21314.

Schmidt, G. A., LeGrande, A. N., and Hoffmann, G. (2007), Water isotope expression of intrinsic and forced variability in a coupled ocean-atmosphere model, *Journal of Geophysical Research*, *112*D10103.

Schmidt, G. A. et al. (2017), Practice and philosophy of climate model tuning across six US modeling centers, *Geoscientific Model Development*, *10*3207-3223.

Sherwood, S. C., Bony, S., and Dufresne, J.-L. (2014), Spread in model climate sensitivity traced to atmospheric convective mixing, *Nature*, *505*37-42.

Sherwood, S. C. et al. (2020), An Assessment of Earth's Climate Sensitivity Using Multiple Lines of Evidence., *Rev Geophys*, *58*(4), e2019RG000678, doi:10.1029/2019RG000678.

Tarasov, L., Dyke, A. S., Neal, R. M., and Peltier, W. R. (2012), A data-calibrated distribution of deglacial chronologies for the North American ice complex from glaciological modeling, *Earth and Planetary Science Letters*, *315-316*30-40.

Tarasov, L., and Peltier, W. R. (2002), Greenland glacial history and local geodynamic consequences, *Geophysical Journal International*, *150*(1), 198-229.

Tian, B., Fetzer, E. J., and Manning, E. M. (2019), TThe Atmospheric Infrared Sounder Obs4MIPs Version 2 Data Set, *Earth and Space Science*, *6*(2), 324-333, doi:10.1029/2018EA000508.

Tian, B., and Hearty, T. (2020), Estimating and removing the sampling biases of the AIRS Obs4MIPs V2 data, *Earth and Space Science*, *7*(12), e2020EA001438.

Tierney, J. E. et al. (2020a), Glacial cooling and climate sensitivity revisited, *Nature*, *584*569-573.

Tierney, J. E. et al. (2020b), Past climates inform our future, *Science*, *370*(6517).

Ullman, D. J., LeGrande, A. N., Carlson, A. E., Anslow, F. S., and Licciardi, J. M. (2014), Assessing the impact of Laurentide Ice Sheet topography on glacial climate, *Climate of the Past*, *10*487-507.

Waliser, D. et al. (2020), Observations for model Intercomparison project (Obs4MIPs): Status for CMIP6, *Geoscientific Model Development*, *13*2945-2958.

Waters, J. W. F., L. Harwood, R.S. Jarnot, R.F. Pickett, H.M. Read, W.G. Siegel, P.H. Cofield, R.E. Filipiak, M.J. Flower, D.A. Holden, J.R. et al. (2006), The earth observing system microwave limb sounder (EOS MLS) on the Aura satellite, *IEEE Transactions on Geoscience and Remote Sensing*, *44*(5), 1075-1092.

Webb, M. J. et al. (2015), The impact of parametrized convection on cloud feedback, *Philosophical Transactions of the Royal Society A: Mathematical, Physical and Engineering Sciences*, *373*(2054), 20140414.

Wentz, F. J., Ricciardulli, L., Hilburn, K., and Mears, C. (2007), How Much More Rain Will Global Warming Bring?, *Science*, *317*(5835), 233-235.

Wentz, F. J., and Schabel, M. (2000), Precise climate monitoring using complementary satellite data sets, *Nature*, *403*414-416.

Werner, M. et al. (2016), Glacial-interglacial changes in H218O, HDO and deuterium excess - results from the fully coupled ECHAM5/MPI-OM Earth system model, *Geoscientific Model Development*, *9*647-670.

Worden, J., Noone, D., Bowman, K. and The Tropospheric Emission Spectrometer science team and data contributors, (2007), Importance of rain evaporation and continental convection in the tropical water cycle, *Nature*, *445*(7127), 528-532.

Yi, B., Rapp, A. D., Yang, P., Baum, B. A., and King, M. D. (2017), A comparison of Aqua MODIS ice and liquid water cloud physical and optical properties between collection 6 and collection 5.1: Cloud radiative effects, *Journal of Geophysical Research: Atmospheres*, *122*(8), 4550-4564.

Zelinka, M. D. et al. (2020), Causes of higher climate sensitivity in CMIP6 models, *Geophysical Research Letters*, *47*(1), e2019GL085782.

Zhu, J. et al. (2021), Assessment of equilibrium climate sensitivity of the Community Earth System Model version 2 through simulation of the Last Glacial Maximum, *Geophysical Research Letters*, *48*(3), e2020GL091220.

Zhu, J., and Poulsen, C. J. (2020), On the increase of climate sensitivity and cloud feedback with warming in the Community Atmosphere Models, *Geophysical Research Letters*, *47*(18), e2020GL089143.

Zhu, J., Poulsen, C. J., and Tierney, J. E. (2019), Simulation of Eocene extreme warmth and high climate sensitivity through cloud feedbacks, *Science Advances*, *5*eaax1874.